

Memory-Efficient 3D High-Resolution Medical Image Synthesis Using CRF-Guided GANs

Mahshid Shiri¹[0009-0008-5780-724X], Alessandro Bruno²[0000-0003-0707-6131],
and Daniele Loiacono¹[0000-0002-5355-0634]

¹ Politecnico di Milano, Department of Electronics, Information, and Bioengineering,
Piazza Leonardo da Vinci, 32, 20133 Milan, Italy.

² IULM University, Department of Business, Law, Economics, and Consumer
Behaviour 'Carlo A. Ricciardi'. Via Carlo Bo, 1. 20143, Milan, Italy.

Abstract. Generative Adversarial Networks (GANs) have many potential medical imaging applications. Due to the limited memory of Graphical Processing Units (GPUs), most current 3D GAN models are trained on low-resolution medical images, these models cannot scale to high-resolution or are susceptible to patchy artifacts. In this work, we propose an end-to-end novel GAN architecture that uses Conditional Random field(CRF) to model dependencies so that it can generate consistent 3D medical Images without exploiting memory. To achieve this purpose, the generator is divided into two parts during training, the first part produces an intermediate representation and CRF is applied to this intermediate representation to capture correlations. The second part of the generator produces a random sub-volume of image using a subset of the intermediate representation. This structure has two advantages: first, the correlations are modeled by using the features that the generator is trying to optimize. Second, the generator can generate full high-resolution images during inference. Experiments on Lung CTs and Brain MRIs show that our architecture outperforms state-of-the-art while it has lower memory usage and less complexity.

Keywords: Medical Imaging · Deep Learning · Generative Adversarial Networks · Conditional Random Fields · 3D Image Synthesis · Memory Efficiency.

1 Introduction

Generative models have gained considerable popularity among researchers for a variety of tasks, including data augmentation[4]. Generative Adversarial Networks (GANs)[7] have made remarkable strides in the biomedical field. These advancements are largely due to recent improvements in computational power and the availability of extensive medical datasets.

3D GAN models were proposed for reducing noise in low-dose CT scans[22], enhancing the quality of CT images[16], generating realistic 3D brain MRI images[13], and creating tumor masks for segmentation[5]. However, these methods have a limitation in the generated image resolution, which is usually 128^3 or smaller, because of limited memory during training[23].

Memory-efficient GANs aim to balance memory efficiency and generative capability, ensuring that GANs can be trained effectively even with limited computational resources. To this aim, the experimental campaigns by Lei et al.[19] and Yu et al.[27] focused on producing new images slice by slice or patch by patch. However, as these methods generate patches and slices independently, the related boundaries may exhibit artefacts. Also, Uzunova et al. [23] use two GANs to generate images, with the first network releasing a lower-resolution version of the image and the second producing higher-resolution patches conditioned on the first GAN. This approach is still patch-based and lacks a comprehensive understanding of the entire image structure. Furthermore, it does not support end-to-end training, making it impractical to use encoders in this context.

Also, Sun et al.[23] proposed an end-to-end hierarchical GAN architecture (HA-GAN), capable of generating high-resolution 3D images at a resolution of 256^3 . The HA-GAN architecture consists of two interconnected GANs: low-resolution GAN that produces a low-resolution version of the 3D image, capturing essential global structure with reduced computational and memory requirements, and high-resolution GAN that generates high-resolution patches for a randomly selected sub-volume of the image. The high-resolution generator shares its initial layers with the low-resolution generator, ensuring consistency and efficient use of memory. During inference, HA-GAN is capable of directly generating full high-resolution 3D images without the need for additional post-processing. HA-GAN demonstrates superior performance compared to state-of-the-art models in generating high-resolution 3D images.

This work aims to address the limitations of existing 3D GAN models by presenting a novel architecture for high-resolution 3D medical image synthesis that combines Conditional Random Fields (CRF) with GANs. The main contribution of this research is the development of a more memory-efficient and high-performing architecture. This study aims to advance the quality and applicability of synthetic medical images by tackling key challenges such as consistency, memory efficiency, model complexity, and performance.

2 Conditional Random Field(CRF)

Conditional Random Field(CRF) is a type of probabilistic graphical model used in machine learning. It tackles dependencies between the output variables, taking into account the data’s sequential or structural nature. CRFs” allow capturing correlations between image patches. Let’s denote the embedding of patches as $x = \{x_i\}_{i=1}^N$, where N represents the number of patches. Each patch i is associated with a random variable $y = \{y_i\}_{i=1}^N$, denoting the binary label of each patch. The conditional distribution $P(Y|x)$ can be formulated as a CRF with a Gibbs distribution, as depicted in Equation 1.

$$P(Y = y | x) = \frac{1}{Z(x)} \exp(-E(y, x)) \quad (1)$$

Here, $E(y, x)$ represents the energy function, quantifying the cost of Y assuming a specific configuration y given x . $Z(x)$ stands for the partition function

ensuring that $P(Y = y|x)$ is a legitimate probability distribution. In the context of a fully-connected pairwise CRF[15], the energy function can be expressed as Equation 2.

$$E(y, x) = \sum_i u(y_i) + \sum_{i < j} p(y_i, y_j) \quad (2)$$

\sum_i and $\sum_{i < j}$ indicate summations over all patches and pairwise combinations of patches, respectively. $u(y_i)$ signifies the unary potential associated with patch i that measures the cost of patch i taking the label y_i given the patch embedding x_i , while $p(y_i, y_j)$ represents the pairwise potential between patches i and j that measures the cost of jointly assigning patch i, j with labels y_i, y_j given the patch embeddings x_i, x_j respectively. Pairwise potential $p(y_i, y_j)$ models spatial correlations between neighboring patches, and would encourage low cost for assigning y_i, y_j with the same label if x_i, x_j are similar[25].

Li et al.[20] incorporate CRF on top of a feature extractor to refine segmentation results and ensure spatial coherence within the image. Zhong[28] explores the combined use of GANs and CRF for hyper-spectral image classification. Zhong[28] employed CRFs as a post processing layer to refine the classification results obtained from GAN-generated hyper-spectral images.

3 Method

In this section, we explain the underlying idea behind the proposed method and the overall architecture.

3.1 Idea Behind Proposed Architecture

When training a GAN, the generator learns different levels of detail across its layers. The initial layers focus on broad, coarse features, while the later layers refine the finer details. The generator starts with a noise vector, progressively adding information with each layer, until the final output is a complete image.

We can split the generator into two parts: the first part generates an embedding that captures the overall structure of the image, and the second part refines this into the full image. The point in the network where we divide the network is critical because the earlier layers are too abstract, and the later layers are too specific. A good division is usually somewhere in the middle, where the output is detailed enough to be informative.

From another perspective, the output of the first layers can be seen as the embedding of the images, which encapsulates the knowledge of the global structure. A common approach in the literature[23,24] to provide more feedback on the first layers regarding the consistency in the final images is to use another GAN. In this work, we capture structures and dependencies by applying CRFs to the embeddings rather than training an additional GAN.

CRFs are lightweight discriminative models that capture correlations between patches without producing extra outputs. They can be integrated into a

simple GAN architecture to provide feedback on the consistency and structures between patches to the generator by analyzing embeddings and their neighbors. Meanwhile, the discriminator assesses how realistic the generated images are by examining patches of the image. This dual feedback mechanism ensures that the generator receives feedback on both consistency and realism.

3.2 Components

Two-Step GAN Structure: As depicted in Fig .1, the generator is structured into two sections to access image embeddings. The initial section (G_1) generates an embedding of images (A) from a noise variable (z). During training, a random subset of the embedding A is selected (A_r) and passed to the second network. During inference, the whole embedding A is passed to the second network to generate full image. The second network (G_2) generates patches of image in full resolution from the selected subset A_r . This selection procedure is also applied to real images (X) prior to their inclusion in the discriminator input. Consequently, the loss function of Generators and Discriminator (D) would be as Equation 3.

$$L_{GAN}(G_1, G_2, D) = \min_{G_1, G_2} \max_D [\mathbb{E}_{r \sim p_r} [\mathbb{E}_{x \sim p_{data}} [\log D(X_{(r:r+constant)})]] + \mathbb{E}_{z \sim p_z} [\log (1 - D(G_2(G_1(z))_{(r:r+constant)}))]]] \quad (3)$$

Half-Encoder Structure: An encoder is integrated into the architecture to acquire a condensed representation of the entire image and prevent mode collapse and it takes patches of images as input. Despite normal encoders, the designed encoder only reverses the procedure of G_2 , so it is referred to as the half-encoder. The output of the encoder is then fed into G_2 for training and subsequently compared with the original patches. The designed encoder is able to generate embedding of both synthetic and real images which is going to be used during training of CRF component. The loss is calculated as Equation 4, where l_1 loss is utilized to achieve sharper results compared to l_2 loss[29].

$$L_{reconstruct}(E) = \min_E [\mathbb{E}_{(x \sim p_{data}, r \sim p_r)} \|X_r - G_2(\widehat{A}_r)\|_1], \text{ where } \widehat{A}_r = E(X_r) \quad (4)$$

3.3 Proposed Architecture (CRF-GAN)

By utilizing the two-step GAN and half-encoder, the embedding of real and synthetic images is provided. As said earlier, this embedding(A) does not illustrate details but contains the general structure of images. To use the information that is encoded into A , CRF is applied to the output of $G_1(A)$ and captures correlations. So, the first section of the generator would receive feedback both from the CRF and the discriminator. In this way, the signal about the general structure is transferred to the generator so that the inconsistency between patches is prevented.

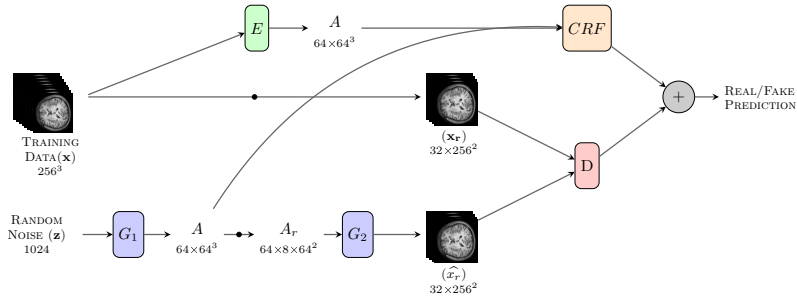


Fig. 1: CRF-GAN architecture. CRF is applied to the embedding of real images(output of E) and synthetic images(output of G_1)

This approach has several advantages. First, the CRF is trained using the same features produced by the generator, secondly, training a CRF incurs significantly less overhead compared to training an extra GAN, resulting in a model with lower complexity than existing memory-efficient GAN architectures. Equation 5 defines the loss function, and Fig. 1 illustrates the architecture.

$$\begin{aligned}
 \mathcal{L}_{\text{CRF-GAN}}(G_1, G_2, D, \text{CRF}) = & \\
 \min_{G_1, G_2} \max_{D, \text{CRF}} & \left[\mathbb{E}_{r \sim p_r} \left[\mathbb{E}_{x \sim p_{\text{data}}} \left[\frac{\log(D(X_{r:r+\text{constant}}) + \text{CRF}(E(X)))}{2} \right] \right] \right. \\
 & \left. + \mathbb{E}_{z \sim p_z} \left[\frac{\log(1 - (D(G_2(G_1(z))_{r:r+\text{constant}}) + \text{CRF}(G_1(z))))}{2} \right] \right] \quad (5)
 \end{aligned}$$

4 Experiments

HA-GAN[23] has demonstrated superior performance compared to baseline methods such as WGAN[9], VAE-GAN[18], α GAN[17], ProgressiveGAN[14], 3D StyleGAN 2[11], and CCE-GAN[26]. Additionally, HA-GAN[23] is the only model capable of generating images with a size of 256³ due to memory constraints. Therefore, the proposed architecture is compared to HA-GAN in this section.

The study utilizes three 3D datasets, namely the GSP dataset[3], the LIDC-IDRI dataset[1], and the dataset employed for the Lung Nodule Analysis 2016 (LUNA16) challenge[21] which is a subset of LIDC-IDRI dataset. Samples from generated images at different stages of training are presented in Fig. 2 and Fig.3.

4.1 Performance Analysis

Within this segment, we outline the selected assessment criteria employed to evaluate the efficiency of the suggested architecture.

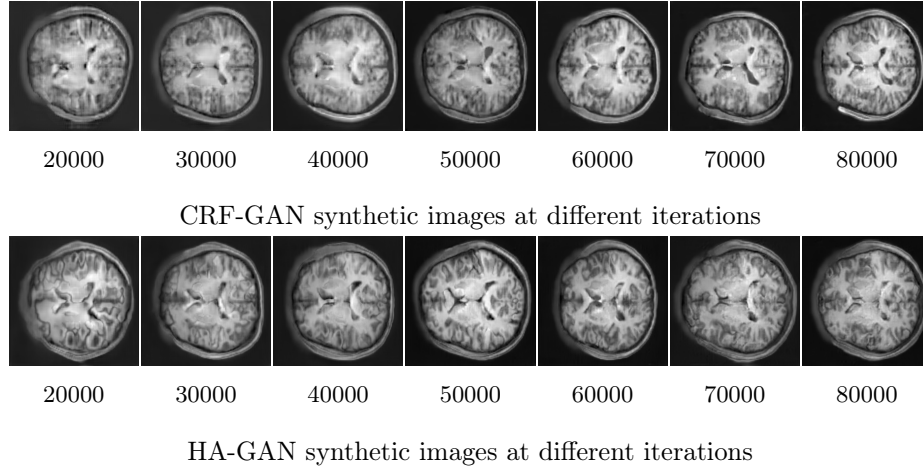


Fig. 2: Synthetic images of CRF-GAN and HA-GAN at different iterations of training on GSP dataset

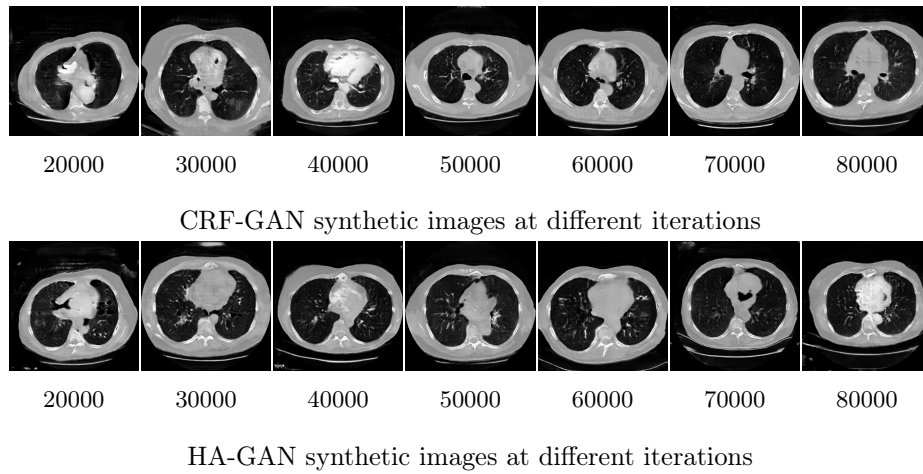


Fig. 3: Synthetic images of CRF-GAN and HA-GAN at different iterations of training on the LUNA16 dataset

FID and MMD Scores: For the purpose of assessment, the metrics of Fréchet Inception Distance (FID)[10] and Maximum Mean Discrepancy (MMD)[8] are computed. FID focuses on quantifying the dissimilarity between the generated and real distributions and captures both precision and recall. On the other hand, MMD differentiate between generated and real images with minimal sample and computational complexity[2]. Lower FID and MMD scores show the proximity of generated images to real images.

To evaluate the performance, a subset comprising 20% of the GSP dataset and 10% of the LUNA16 dataset was designated as test data and the experiments are done on 256^3 resolution. The resulting scores are tabulated in Table 1. Notably, CRF-GAN achieved better FID and superior MMD scores across both datasets, underscoring its efficacy in generating images closely resembling real images.

Table 1: FID and MMD scores computed on the 256^3 resolution images of GSP and LUNA16 dataset. As lower FID and MMD scores outline better image fidelity, it can be seen that CRF-GAN achieved better results.

Models	GSP dataset		LUNA16 dataset	
	FID ↓	MMD ↓	FID ↓	MMD ↓
HA-GAN	0.009278	0.003802	0.061021	0.086461
CRF-GAN	0.007044	0.000099	0.047062	0.084015

Simplicity: We explored the simplicity of CRF-GAN and HA-GAN models by analyzing the total number of learnable parameters at different resolutions, which are presented in Table 2. The proposed architecture demonstrates a reduction in parameters at each resolution, with decreases of 27.4%, 28.1%, and 28.2% observed for resolutions 64^3 , 128^3 , and 256^3 respectively.

Table 2: The total number of learnable parameters for CRF-GAN and HA-GAN at varying resolutions in millions (M).

Resolution	#Parameters	
	CRF-GAN	HA-GAN
64^3	57.07 M	78.7 M
128^3	57.20 M	79.58 M
256^3	57.24 M	79.74 M

Memory Efficiency: We captured the maximum memory allocated during training. This procedure was performed on batch sizes of 2, 4 and 6 on both 128^3

and 256^3 resolutions. The results are outlined in Table 3. HA-GAN consistently used more memory than CRF-GAN at both 128^3 and 256^3 resolutions across all batch sizes. The memory usage disparity increased with higher batch sizes, with HA-GAN averaging about 9.4% more memory usage than CRF-GAN.

Table 3: Memory usage of HA-GAN and CRF-GAN for different batch sizes at 128^3 and 256^3 resolutions. "-" indicates that the models exploit GPU's memory.

Models	Max Memory allocated (MB)					
	128^3			256^3		
	2	4	6	2	4	6
HA-GAN	2812	2984	3098	7710	10434	-
CRF-GAN	2622	2712	2774	7494	9010	-

Training Speed: In addition, we measured the number of iterations per second during training, setting the batch size to 2. CRF-GAN is approximately 14.6%, 10.2% faster than HA-GAN at 128^3 , 256^3 spatial resolutions respectively, as shown in Table 4.

Table 4: Training speed (iter/sec) for CRF-GAN and HA-GAN.

Resolution	Training speed (iter/sec)	
	CRF-GAN	HA-GAN
128^3	1.394	1.216
256^3	4.236	3.845

Augmentation Task: Frid-Adar et al.[6] demonstrated that GAN-generated samples enhance training dataset diversity and improve classifier's performance. To investigate the potential of synthetic images, we extended our CRF-GAN architecture for conditional image generation and designed a binary classification task. To this end, we used a subset of the LIDC-IDRI dataset, categorizing images into two classes: positive (nodules rated 5, high malignancy likelihood) and negative (no nodules).

The classifier was trained under three configurations: 1) using only real data, 2) using a 50-50 mix of real and CRF-GAN synthetic images, and 3) using a 50-50 mix of real and HA-GAN synthetic images. Each configuration was trained with 10 different seeds, and the average performance metrics are shown in Table 5. The dataset was imbalanced, with a higher number of scans containing nodules compared to those without.

To compare both architectures more fairly, we allowed the classifier to learn until early stopping was triggered based on the validation loss, rather than training the classifiers for a fixed number of iterations as done in [23]. This approach lets the classifier use the provided data until performance plateaus, allowing us to better assess the impact of adding synthetic images.

The classifier with CRF-GAN synthetic images achieved the highest recall (79.99%), indicating lower false negative cases. Precision values were high for both CRF-GAN (78.55%) and HA-GAN (79.02%), showing low false positive rates. The CRF-GAN classifier had the highest F1 score (79.21%), indicating a good balance between precision and recall. The standard deviations for the precision, recall, and F1 scores across all configurations indicate variability in the model’s performance, with CRF-GAN showing lower variability compared to HA-GAN, suggesting more consistent results.

In medical imaging, especially with critical conditions like nodules, it is crucial to prioritize models with higher recall to ensure fewer missed diagnoses. CRF-GAN’s strength lies in its higher recall and F1 score, indicating that the synthetic images generated by CRF-GAN enhance the model’s ability to detect nodules, despite some increase in false positives. This is generally preferable in medical imaging, where false negatives are more critical than false positives. On the other hand, HA-GAN’s high precision but low recall and F1 score suggest that while the synthetic images from HA-GAN help avoid false positives, they fail to improve the model’s ability to detect nodules.

Table 5: Average classifier performance trained with real data and, real + synthetic data of CRF-GAN and real + synthetic data of HA-GAN.

Configuration	Precision (%)	Recall (%)	F1 Score (%)
Baseline	76.97 \pm 2.34	77.27 \pm 9.06	76.92 \pm 5.27
With CRF-GAN	78.55 \pm 1.99	79.99 \pm 5.19	79.21 \pm 3.19
With HA-GAN	79.02 \pm 2.42	73.33 \pm 7.8	75.79 \pm 3.63

5 Conclusion

We presented a novel memory-efficient GAN architecture that showcases significant progress in generating high-resolution 3D medical images. By utilizing CRF to model dependencies within the intermediate representations generated by the generator, this architecture effectively addresses the limitations imposed by the limited memory capacity of GPUs.

The experimental findings on Lung CTs and Brain MRIs confirm the advantage of this approach compared to state-of-the-art methods, highlighting its lower memory usage, reduced complexity, and improved performance of existing models. However, the incorporation of CRF contributes to smoother results that require further attention in future studies.

To evaluate the proposed model, we utilized both FID and MMD scores. FID is a well-known metric for measuring the quality of generated images, but its reliability can be limited in certain situations [12]. For this reason, we also incorporated the MMD score as an additional evaluation metric. Furthermore, we examined the effectiveness of our model through data augmentation, which showed enhanced performance compared to existing models.

We also conducted a preliminary evaluation with medical experts to assess the clinical realism of the generated images. The initial feedback was encouraging, and we plan to expand on this analysis in future work.

References

1. Armato III, S.G., McLennan, G., Bidaut, L., McNitt-Gray, M.F., Meyer, C.R., Reeves, A.P., Zhao, B., Aberle, D.R., Henschke, C.I., Hoffman, E.A., et al.: The lung image database consortium (lidc) and image database resource initiative (idri): a completed reference database of lung nodules on ct scans. *Medical physics* **38**(2), 915–931 (2011)
2. Borji, A.: Pros and cons of gan evaluation measures. *Computer vision and image understanding* **179**, 41–65 (2019)
3. Buckner, R.L., Roffman, J.L., Smoller, J.W.: Brain Genomics Superstruct Project (GSP) (2014). <https://doi.org/10.7910/DVN/25833>, <https://doi.org/10.7910/DVN/25833>
4. Celard, P., Iglesias, E.L., Sorribes-Fdez, J.M., Romero, R., Vieira, A.S., Borrajo, L.: A survey on deep learning applied to medical images: from simple artificial neural networks to generative models. *Neural Computing and Applications* **35**(3), 2291–2323 (2023)
5. Cirillo, M.D., Abramian, D., Eklund, A.: Vox2vox: 3d-gan for brain tumour segmentation. In: *Brainlesion: Glioma, Multiple Sclerosis, Stroke and Traumatic Brain Injuries: 6th International Workshop, BrainLes 2020, Held in Conjunction with MICCAI 2020, Lima, Peru, October 4, 2020, Revised Selected Papers, Part I* 6. pp. 274–284. Springer (2021)
6. Frid-Adar, M., Diamant, I., Klang, E., Amitai, M., Goldberger, J., Greenspan, H.: Gan-based synthetic medical image augmentation for increased cnn performance in liver lesion classification. *Neurocomputing* **321**, 321–331 (2018)
7. Goodfellow, I., Pouget-Abadie, J., Mirza, M., Xu, B., Warde-Farley, D., Ozair, S., Courville, A., Bengio, Y.: Generative adversarial nets. *Advances in neural information processing systems* **27** (2014)
8. Gretton, A., Borgwardt, K.M., Rasch, M.J., Schölkopf, B., Smola, A.: A kernel two-sample test. *The Journal of Machine Learning Research* **13**(1), 723–773 (2012)
9. Gulrajani, I., Ahmed, F., Arjovsky, M., Dumoulin, V., Courville, A.C.: Improved training of wasserstein gans. *Advances in neural information processing systems* **30** (2017)
10. Heusel, M., Ramsauer, H., Unterthiner, T., Nessler, B., Hochreiter, S.: Gans trained by a two time-scale update rule converge to a local nash equilibrium. *Advances in neural information processing systems* **30** (2017)
11. Hong, S., Marinescu, R., Dalca, A.V., Bonkhoff, A.K., Bretzner, M., Rost, N.S., Golland, P.: 3d-stylegan: A style-based generative adversarial network for generative modeling of three-dimensional medical images. In: *Deep Generative Models, and Data Augmentation, Labelling, and Imperfections: First Workshop*,

- DGM4MICCAI 2021, and First Workshop, DALI 2021, Held in Conjunction with MICCAI 2021, Strasbourg, France, October 1, 2021, Proceedings 1. pp. 24–34. Springer (2021)
12. Jayasumana, S., Ramalingam, S., Veit, A., Glasner, D., Chakrabarti, A., Kumar, S.: Rethinking fid: Towards a better evaluation metric for image generation. In: Proceedings of the IEEE/CVF Conference on Computer Vision and Pattern Recognition. pp. 9307–9315 (2024)
 13. Jin, W., Fatehi, M., Abhishek, K., Mallya, M., Toyota, B., Hamarneh, G.: Applying artificial intelligence to glioma imaging: Advances and challenges. arXiv preprint arXiv:1911.12886 pp. 1–31 (2019)
 14. Karras, T., Aila, T., Laine, S., Lehtinen, J.: Progressive growing of gans for improved quality, stability, and variation. arXiv preprint arXiv:1710.10196 (2017)
 15. Krähenbühl, P., Koltun, V.: Efficient inference in fully connected crfs with gaussian edge potentials. *Advances in neural information processing systems* **24** (2011)
 16. Kudo, A., Kitamura, Y., Li, Y., Iizuka, S., Simo-Serra, E.: Virtual thin slice: 3d conditional gan-based super-resolution for ct slice interval. In: Machine Learning for Medical Image Reconstruction: Second International Workshop, MLMIR 2019, Held in Conjunction with MICCAI 2019, Shenzhen, China, October 17, 2019, Proceedings 2. pp. 91–100. Springer (2019)
 17. Kwon, G., Han, C., Kim, D.s.: Generation of 3d brain mri using auto-encoding generative adversarial networks. In: International Conference on Medical Image Computing and Computer-Assisted Intervention. pp. 118–126. Springer (2019)
 18. Larsen, A.B.L., Sønderby, S.K., Larochelle, H., Winther, O.: Autoencoding beyond pixels using a learned similarity metric. In: International conference on machine learning. pp. 1558–1566. PMLR (2016)
 19. Lei, Y., Wang, T., Liu, Y., Higgins, K., Tian, S., Liu, T., Mao, H., Shim, H., Curran, W.J., Shu, H.K., et al.: Mri-based synthetic ct generation using deep convolutional neural network. In: Medical Imaging 2019: Image Processing. vol. 10949, pp. 716–721. SPIE (2019)
 20. Li, Y., Ping, W.: Cancer metastasis detection with neural conditional random field. arXiv preprint arXiv:1806.07064 (2018)
 21. Setio, A.A.A., Traverso, A., De Bel, T., Berens, M.S., Van Den Bogaard, C., Cerello, P., Chen, H., Dou, Q., Fantacci, M.E., Geurts, B., et al.: Validation, comparison, and combination of algorithms for automatic detection of pulmonary nodules in computed tomography images: the luna16 challenge. *Medical image analysis* **42**, 1–13 (2017)
 22. Shan, H., Zhang, Y., Yang, Q., Kruger, U., Kalra, M.K., Sun, L., Cong, W., Wang, G.: 3-d convolutional encoder-decoder network for low-dose ct via transfer learning from a 2-d trained network. *IEEE transactions on medical imaging* **37**(6), 1522–1534 (2018)
 23. Sun, L., Chen, J., Xu, Y., Gong, M., Yu, K., Batmanghelich, K.: Hierarchical amortized gan for 3d high resolution medical image synthesis. *IEEE journal of biomedical and health informatics* **26**(8), 3966–3975 (2022)
 24. Uzunova, H., Ehrhardt, J., Jacob, F., Frydrychowicz, A., Handels, H.: Multi-scale gans for memory-efficient generation of high resolution medical images. In: Medical Image Computing and Computer Assisted Intervention–MICCAI 2019: 22nd International Conference, Shenzhen, China, October 13–17, 2019, Proceedings, Part VI 22. pp. 112–120. Springer (2019)
 25. Wallach, H.M., et al.: Conditional random fields: An introduction. Tech. rep., Technical reports (CIS) (2004)

26. Xing, S., Sinha, H., Hwang, S.J.: Cycle consistent embedding of 3d brains with auto-encoding generative adversarial networks. In: *Medical Imaging with Deep Learning* (2021)
27. Yu, B., Zhou, L., Wang, L., Fripp, J., Bourgeat, P.: 3d cgan based cross-modality mr image synthesis for brain tumor segmentation. In: *2018 IEEE 15th international symposium on biomedical imaging (ISBI 2018)*. pp. 626–630. IEEE (2018)
28. Zhong, Z.: Spectral-spatial neural networks and probabilistic graph models for hyperspectral image classification (2019)
29. Zhu, J.Y., Park, T., Isola, P., Efros, A.A.: Unpaired image-to-image translation using cycle-consistent adversarial networks. In: *Proceedings of the IEEE international conference on computer vision*. pp. 2223–2232 (2017)